Check for updates

JGR Planets

RESEARCH ARTICLE
10.1029/2022JE007633

Key Points:

- We map and characterize 10 fault groups in Ulysses Fossae; the majority of the fault groups are interpreted to be initiated by radial diking
- We present an overview of the volcano-tectonic history of the area constraining relative and absolute ages using crater frequency analysis
- The majority of the faulting takes place during the Early Amazonian and reflects an active diking system in Tharsis during this period

Supporting Information:

Supporting Information may be found in the online version of this article.

Correspondence to:

S. Shahrzad,
eessha@leeds.ac.uk

Citation:

Shahrzad, S., Bramham, E. K., Thomas, M., Piazolo, S., Byrne, P. K., & Mortimer, E. (2023). Deciphering the structural history of Ulysses Fossae, Mars, using fault pattern analysis. *Journal of Geophysical Research: Planets*, *128*, e2022JE007633. https://doi.org/10.1029/2022JE007633

Received 18 OCT 2022
Accepted 27 APR 2023

© 2023. The Authors.
This is an open access article under the terms of the Creative Commons Attribution License, which permits use, distribution and reproduction in any medium, provided the original work is properly cited.

Deciphering the Structural History of Ulysses Fossae, Mars, Using Fault Pattern Analysis

Stephanie Shahrzad[1], Emma K. Bramham[1], Mark Thomas[1], Sandra Piazolo[1], Paul K. Byrne[2], and Estelle Mortimer[1]

[1]School of Earth and Environment, University of Leeds, Leeds, UK, [2]Department of Earth and Planetary Science, Washington University in St. Louis, St. Louis, MO, USA

Abstract Ulysses Fossae is a faulted region surrounded by lava flows that sits between the major volcanoes of the Tharsis Rise volcanic province on Mars. This area is unique, as it is the only exposure of extensional faulting which can be related to the Olympus Mons volcano and one of the only a few faulted areas relating to the Tharsis Montes. In order to determine the area's structural evolution through time, we mapped all identifiable faults, divided them into 10 fault groups determined by their orientation and morphology, and performed detailed crater size-frequency analysis of the geological units. We divide the fault groups into two overall types based on their genesis: local diking and regional extension. The complex structural evolution recorded in the extensional faults in Ulysses Fossae is dominated by local dike-related activity (8/10 fault groups), along with deformation from large, regional scale extensional processes related to the development of the Tharsis province as a whole (2/10 fault groups). Strain values measured across the 1 fault groups vary between 0.4%–2.2%, with the grabens related to regional extension accommodating larger extensional strains than the local dike-related grabens. The crater size-frequency distribution analysis of three distinct areas in Ulysses Fossae (UF Dome, UF North, and UF South) revealed that the majority of the faulting in Ulysses Fossae was active during the Early Amazonian.

Plain Language Summary The volcanoes in the Tharsis province on Mars are normally associated with deformation of the surface near them and with the growth and development of the volcano. However, in Tharsis, due to its significant coverage of lava, we only find volcanically associated surface deformation for some of the Tharsis volcanoes in an area called Ulysses Fossae. In this study, we map and characterize the surface structures in Ulysses Fossae, which are then used to define the structural history of the area. Our work reveals that there are 10 distinct episodes of deformation in Ulysses Fossae, where most of the activity responsible for the surface structures are associated with subsurface activity from nearby volcanoes. Two of the episodes also show signs of movement associated with the development of the Tharsis region as a whole. Additionally, we determined the ages of this deformation and found that most of the activity takes place during the Amazonian period (~3 billion years ago) in Mars' geologic history. This shows that the volcanic systems surrounding Ulysses Fossae were active for longer than previously determined and together with the mapped structures and provides a detailed history of the different stages of activity in the area.

1. Introduction

The majority of tectonic structures on Mars are believed to be driven by volcanic processes (e.g., Barlow, 2008; Bouley et al., 2018; Carr & Head, 2010). While we do have an understanding of the influence of large-scale stresses in the Tharsis volcanic province (e.g., Bouley et al., 2018; Thomas & Allemand, 1993), we still lack a thorough analysis of the impact of individual volcanoes, and their interactions on surface tectonic structures on Mars. The far-field stresses associated with volcanic centers on Mars thus remain to be fully characterized. For instance, even though the largest volcano in the Solar System, Olympus Mons, has been studied extensively (e.g., De Blasio, 2018; McGovern et al., 2004; Morris & Tanaka, 1994), it is unclear how its presence has influenced the Tharsis-related far-field stress in its surrounding region. Questions such as why there is a considerable difference between the number and size of structures related to different volcanoes with similar plume-induced sources remain. A complicating factor is that the majority of these volcano-related structures are exposed only in restricted patches surrounded by Amazonian lavas. An example of this is Ulysses Fossae, which provides a "window" into some of the volcano-tectonic structures which lay beneath the extensive lava covering Tharsis. Moreover, given how tectonically deformed the entire Tharsis Rise is (e.g., Bouley et al., 2018; E. D. Scott

et al., 2002; Wilson & Head III, 2002), it is unclear to what extent given populations of extensional structures might be attributed to the much large (>2.9 × 10^{12} m^3 (Plescia, 2004)) volcanoes in the region. It is therefore likely that aspects of the tectonic history of Tharsis and other volcanic centers on Mars such as Elysium are more intricate than current models acknowledge (e.g., Anderson et al., 2001; Bouley et al., 2018), where complex faulting patterns are commonly grouped together as a part of a single tectonic stage. Understanding this complexity within Tharsis is essential if we are to decipher the volcano-tectonic history of Mars as a whole, and with that its evolution through time, with accompanying geologic, biological, and atmospheric consequences (Bouley et al., 2018). Unraveling how different faults relate to different volcanoes through time is a fundamental step toward a more nuanced understanding of Tharsis' evolution.

The volcanotectonic province of Tharsis hosts 5 major volcanoes: Olympus Mons, Alba Mons, and the Tharsis Montes (Arsia, Pavonis, and Ascraeus Mons)–and therefore offers a useful case study area to explore the contribution of volcanic edifices to far-field stresses and resultant tectonic structures. The magmatic-driven processes are attributed to the Tharsis Superplume, where its five stages of pulses developed local- and regional scale centers of tectonic activity (Dohm et al., 2007). Plume associated extensional deformation in Tharsis created a suite of diagnostic landforms, with the most common being extensive fault and rift systems, and local and regional centers of magmatic driven activity, producing volcanoes and associated radial and circumferential fault systems (Dohm et al., 2007). The radial fault systems are attributed to dike from one of these local volcanic centers (e.g., Anderson et al., 2001; Dohm et al., 2007), while the commonly observed north-south oriented faults in Tharsis are attributed to isostasy in the first phase of Tharsis' evolution (Banerdt et al., 1982). The volcanic construction on Mars, a single-plate planet. allows the volcanic material to remain vertically above the subsurface source. Isostatic uplift is then generated when the volume of erupted volcanic material moves beyond its source in the Tharsis Region (Banerdt et al., 1982). According to Banerdt et al. (1982), significant uplift will be generated with the removal of only a fraction of volcanic material. This process thus facilitates the tensile hoop stresses identified in Tharsis, responsible for the north-south oriented faulting (Banerdt et al., 1982).

The long-lived Noachian to Amazonian tectonic activity in the Tharsis province has produced widespread extensional faulting (e.g., Mège & Masson, 1997; Scott et al., 2002; Wilson & Head III, 2002). The Alba Mons volcano and its associated extensive fossae systems are perhaps the most obvious manifestation of this deformation (e.g., Bouley et al., 2018; Wilson & Head III, 2002). However, the same extensive fault patterns are not found surrounding other Tharsis volcanoes, such as Olympus Mons. In fact, the only exposed faulting close to Olympus Mons and a handful of other Tharsis volcanoes are found in the Ulysses Fossae area east of the edifice (Figure 1a). Ulysses Fossae has been the target of only a few dedicated studies (Fernández & Ramírez-Caballero, 2019; Scott & Dohm, 1990); yet the preservation of structures in this area holds the potential to unravel the complex deformation history surrounding some of the major Tharsis volcanoes (Figure 1a).

In this study, we undertook an in-depth volcano-tectonic investigation of Ulysses Fossae to illuminate the complex deformation history of the region around the Olympus Mons volcano. We present detailed fault mapping at high spatial resolution, analysis of fault morphology and orientation, strain calculations, and new absolute model ages for geological units in Ulysses Fossae. We use these to present a history of faulting throughout the area, including tracing fault groups to their likely source. By determining, for the first time, the relative ages that is, sequence, absolute ages, and character of faults in the Ulysses Fossae region, we are able to assess the influence and activity of the major volcanic centers in its vicinity—in particular, Olympus Mons, Pavonis Mons and Ulysses Patera.

1.1. The Ulysses Fossae Study Area

The heavily faulted terrain of Ulysses Fossae is located on the Tharsis Rise at 10°N, 123°W, covering 170,840 km^2. It is flanked by a number of large volcanoes, with Olympus Mons situated to the west, the three Tharsis Montes volcanoes to the southeast, and the Ulysses Patera and Biblis Patera volcanoes immediately to the south (Figure 1a).

The geology of the region was initially mapped by Scott et al. (1986) on Viking mission data (130–300 m/pixel), and assigned to the units Hf, defined as "younger fractured material," and Nf, which is "older fractured material." Crater size-frequency distribution calculations determined the age of the Hf unit to be Hesperian, between 3.0 and 3.7 Ga (Scott et al., 1986). In 2014, the units were remapped in a global Mars study by Tanaka et al. (2014), where two different geological units across three distinct areas were identified in Ulysses Fossae, which are the

21699100, 2023, 5, Downloaded from https://agupubs.onlinelibrary.wiley.com/doi/10.1029/2022JE007633 by Test, Wiley Online Library on [20/07/2023]. See the Terms and Conditions (https://onlinelibrary.wiley.com/terms-and-conditions) on Wiley Online Library for rules of use; OA articles are governed by the applicable Creative Commons License

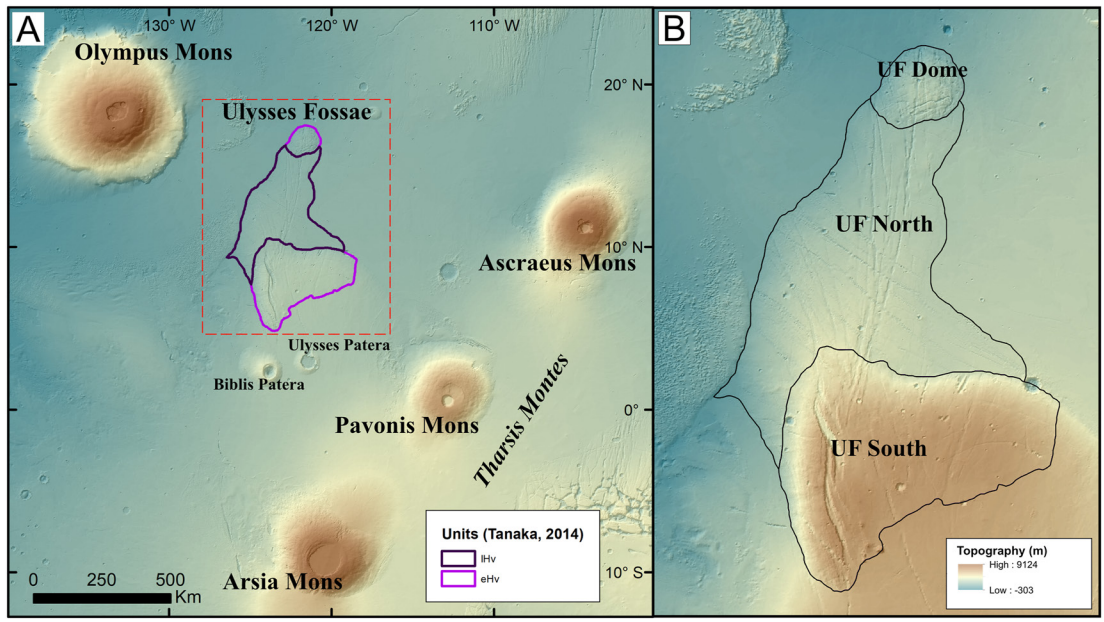

Figure 1. (a) The location of the study area (Ulysses Fossae) and the surrounding Tharsis volcanoes. The central location of the study area between the Tharsis volcanoes Olympus Mons, Pavonis Mons and Ulysses Patera is highlighted in a dashed red line. Note the delineation of Hesperian units lHv and eHv in purple and pink, as mapped by Tanaka et al. (2014). Mars Orbiter Laser Altimeter colorized hillshade is used as background. (b) Names for the 3 areas of Ulysses Fossae. The northern eHv unit is referred to as the "UF Dome," the lHv unit is "UF North" and the southern eHv unit is "UF South."

unit outlines used for this study. These units are eHv (early Hesperian) and lHv (late Hesperian), which are interpreted as undifferentiated lava, most likely from flood lava or large volcanic lava flow (Tanaka et al., 2014). The northernmost section of Ulysses Fossae is characterized by a dome-like structure with a diameter of ∼100 km (UF Dome, Figure 1b). Previous mapping by Scott et al. (1986) described the dome as being highly deformed, older fractured terrain material, distinguishable from the younger southern terrain by a more highly faulted and fractured appearance (Scott & Dohm, 1990). In the Tanaka et al. (2014) mapping, the UF Dome is assigned the unit eHv (Figure 1a). The second region of the eHv unit, as mapped by Tanaka et al. (2014), is to the south and hosts a large sigmoidal fault feature (UF South, Figure 1b). Between the two eHv units lies the late Hesperian lHv unit (UF North, Figure 1b), in which the main characteristic is the continuous linear normal faults crossing the terrain, without the more deformed structures apparent in the UF Dome.

The entire area of Ulysses Fossae, and in particular UF South, sits at a higher elevation than its surroundings (Figure 1b). This has spared Ulysses Fossae from some of the Amazonian lava that have flooded the region, and the area has as a result been able to preserve any features which may have been covered on the rest of this region of Tharsis.

As mentioned, the sources of the faults within Ulysses Fossae have been investigated as a part of only two previous studies. A study by Scott and Dohm (1990) mapped the faults in Ulysses Fossae on Viking photomosaics at 1:2,000,000 scale and assigned their fault groups to proximal volcanoes based on their orientation and age. More recently, Fernández and Ramírez-Caballero (2019) performed a thorough investigation of the large, sigmoidal fault structure south of Ulysses Fossae, which they attributed to oblique rifting.

2. Methods and Data

2.1. Fault Mapping and Grouping

We mapped faults in Ulysses Fossae using images from the Context Camera (CTX) with a resolution of 6 m/pixel (Malin et al., 2007) at a scale of ∼1:250,000 to 1:100,000 in Esri ArcMap software (Figures 2a and 2b). The intention of the mapping was to capture each fault trend, and not to map every single feature. We used the unit boundaries as mapped by Tanaka et al. (2014) to define our study area and confined our fault mapping to these units. However, we captured the full length of a fault if it originated within a unit boundary but continued beyond.

21699100, 2023, 5, Downloaded from https://agupubs.onlinelibrary.wiley.com/doi/10.1029/2022JE007633 by Test, Wiley Online Library on [20/07/2023]. See the Terms and Conditions (https://onlinelibrary.wiley.com/terms-and-conditions) on Wiley Online Library for rules of use; OA articles are governed by the applicable Creative Commons License

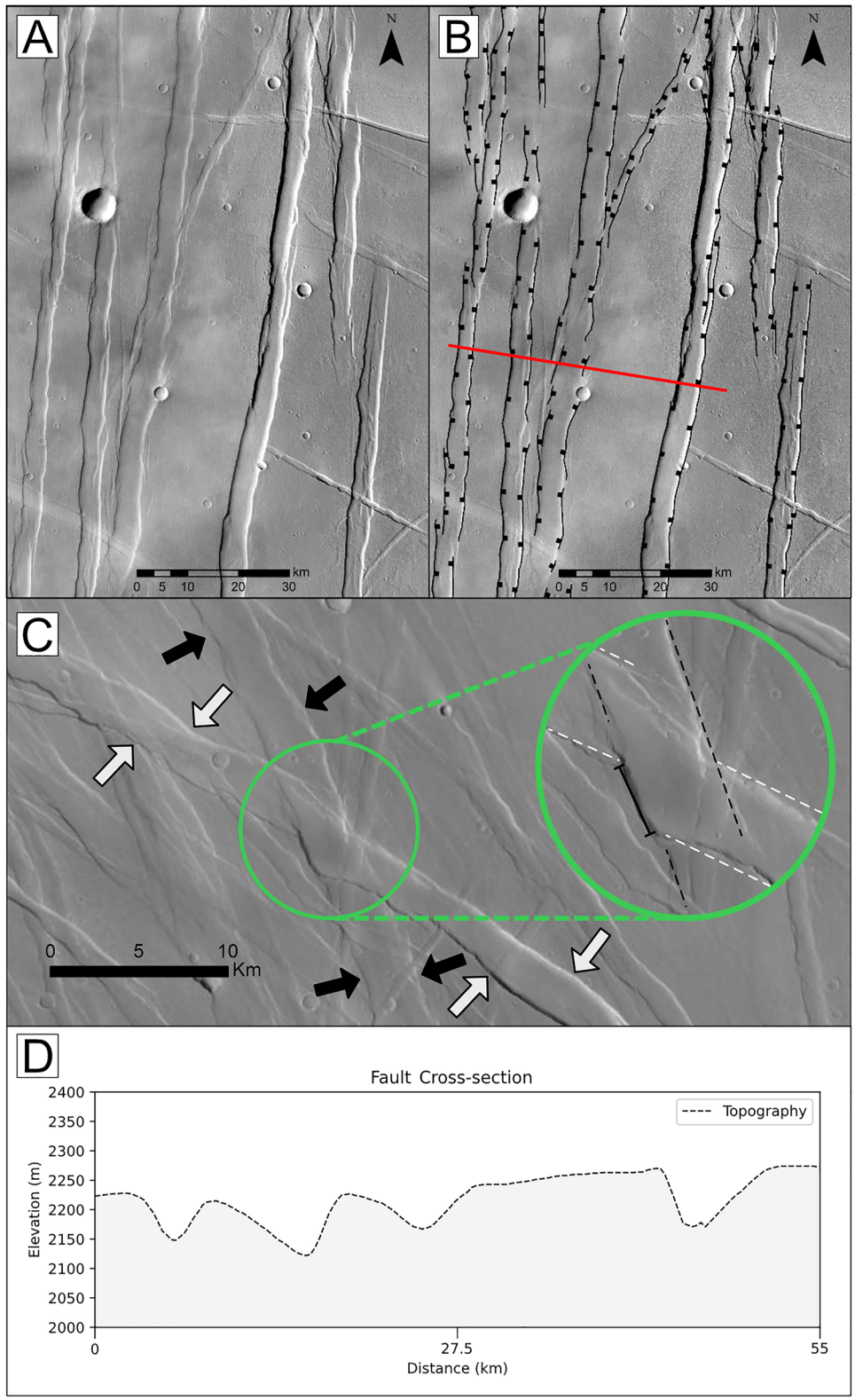

Figure 2. Fault mapping methodology examples. A, (unmapped) and B (mapped) show an example of fault mapping, with (b) showing a red line representing the location for the cross-section in (d). (c) Example of relative age determination based on cross-cutting relationships. The NW-SE fault highlighted by white arrows is clearly offset (Green circle) by the older faults, outlined by black arrows. Zoom in the green circle highlights the displacement (black solid line). (d) Example of cross-section of fault bounding grabens.

21699100, 2023, 5, Downloaded from https://agupubs.onlinelibrary.wiley.com/doi/10.1029/2022JE007633 by Test, Wiley Online Library on [20/07/2023]. See the Terms and Conditions (https://onlinelibrary.wiley.com/terms-and-conditions) on Wiley Online Library for rules of use; OA articles are governed by the applicable Creative Commons License

Fault length and strike orientation were calculated as geodesic lengths and geodesic azimuths with the Tools for Graphics and Shapes plugin for ArcGIS (Jenness, 2011). We also used the FracPaQ software package (Healy et al., 2017) to visualize fault strikes as rose diagrams. For the purposes of this study, we considered hard-linked faults as single continuous faults, whereas soft-linked faults (as defined by Polit et al. (2009)) are considered to be separate, unique faults. Any fault lengths and strikes are thus based on their mappable surface expression, and not on assumed subsurface linkage. Fault intensity is also visualized using FracPaQ, where fault intensity (m^{-1}) is defined as the total length of a fault in a given area. The FracPaQ program generates a 2D grid of circular scan windows over the study area, and the mapped fault intensity is determined using the number of faults intersecting the perimeter of a scan circle (Healy et al., 2017). We use a scan circle diameter of ∼13 km in order to have sufficient detail to capture the complexity of the faulting in the area within the mapped scale.

Following the initial fault mapping, we assigned all the faults to groups. We based our initial grouping on similarity in strike orientation, as calculated and visualized in FracPaQ. These groupings were then subsequently refined by grouping faults with similar morphology and considering the cross-cutting relationships between faults (Figure 2c). This process ensured that each fault group represented a population of faults with a similar age and from a proposed similar origin.

2.2. Chronological Sequence of Faulting

In order to establish the ages of the defined fault groups, we first considered the relative ages between each fault group, and then their absolute ages. Relative ages of fault groups were determined as a function of their cross-cutting relationships, both to the geological units and to other fault groups. For example, where the path of a younger fault is kinked as a result of moving through a pre-existing older fault (Figure 2c). For situations where two given fault groups did not appear to interact with each other, they were put into a relative chronological order based on their relationships to other fault groups as well as their morphology. The absolute ages of the faults were determined by their cross-cutting relationships with the geological units, which have ages assigned from our crater size-frequency distribution analysis (see Section 2.3). This provided a maximum age for the fault group that superposes the unit. If a fault group crossed multiple units with different ages, which was almost always the case, the youngest cross-cut unit age was assigned to the group.

2.3. Crater Size-Frequency Distribution Analysis

To further refine unit ages from the global-scale work of Tanaka et al. (2014), we undertook an independent crater size-frequency distribution analysis of the three Ulysses Fossae areas. We manually identified craters in CTX images and recorded their size and location using the Cratertools application in ArcMap (Kneissl et al., 2011). We only considered craters ≥1 km in diameter in our age analysis in order to avoid the inclusion of secondary impact craters, which can artificially increase the model age (Werner et al., 2009). To ensure no 1 km craters were missed during mapping, we mapped craters down to ∼800 m diameter but did not analyze craters <1 km. The Craterstats v.2 program (Michael, 2013; Michael & Neukum, 2010) was used to determine the absolute model age from crater statistics. In this study, we used the Hartmann and Daubar (2016) production function for Mars, along with the chronology function of Hartmann (2005), with the lower diameter boundary for our crater data set as 1 km. We used the differential plot type, 4th root-2 binning, and a Poisson distribution fit for our statistical data (Michael et al., 2016).

2.4. Strain

To investigate the evolution of extension with time and further compare the fault groups, we measured the maximum finite strain for each fault group. We used topographic measurements taken from profiles (Figure 2d) through the blended global Digital Elevation Model (DEM) derived from the Mars Orbiter Laser Altimeter (MOLA) and High-Resolution Stereo Camera instruments (Fergason et al., 2018). These elevation data have a vertical and horizontal resolution of 1 m/px and 463 m/pixel, respectively (Fergason et al., 2018).

We selected profile locations for each group so that each profile was oriented perpendicular to the main trend of the given fault group and positioned such that the profiles captured the highest fault density while avoiding craters and other non-fault structures. The number of profiles for each group was determined by the quality of the

21699100, 2023, 5, Downloaded from https://agupubs.onlinelibrary.wiley.com/doi/10.1029/2022JE007633 by Test, Wiley Online Library on [20/07/2023]. See the Terms and Conditions (https://onlinelibrary.wiley.com/terms-and-conditions) on Wiley Online Library for rules of use; OA articles are governed by the applicable Creative Commons License

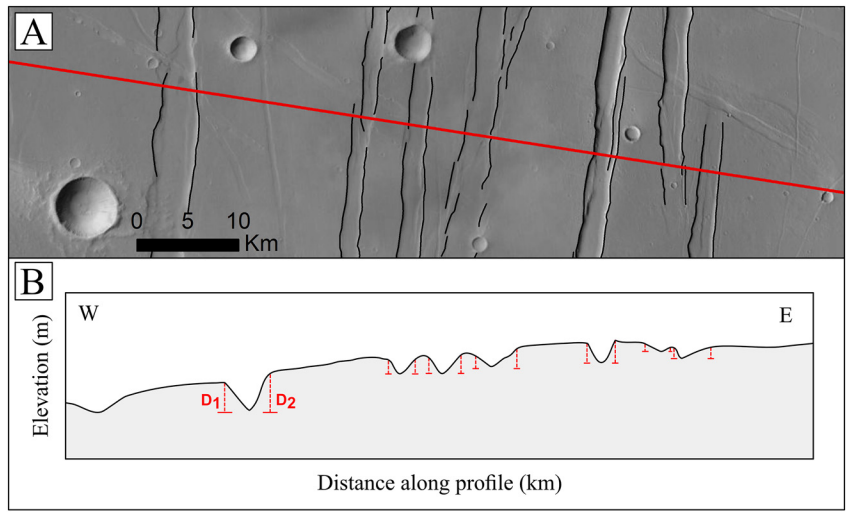

Figure 3. Examples of topographic measurements acquired for strain calculation. (a) Map view of faults in black, and the topographic profile location in red. (b) Example topographic profile created from the Mars Orbiter Laser Altimeter elevation data for Profile B, shown as the red line in (a). Example throw measurement approaches are shown as red dotted lines on the elevation profile, and are labeled D1, D2.

DEM data in the region covered by each group, to ensure each profile line could sufficiently resolve the mapped faults. See Data Set S1 for the X, Y coordinates for the profiles. The topographic profiles were extracted from the HRSC-MOLA DEMs using QGIS software.

From the topographic profiles, we first calculated the extension by measuring the height of each fault scarp for the intersected graben-bounding faults, providing a throw (D_n) value. To convert throw into horizontal displacement, we assumed a 60° fault dip, consistent with Martian estimations for normal faults (e.g., Hauber & Kronberg, 2005; Polit et al., 2009). Figure 3 highlights an example of measuring the throw of the faults along a profile.

Following the method by Hauber and Kronberg (2005), the cumulative extension along the mapped profiles for each fault population was calculated by

$$e_{\text{cum}} = \frac{D_{\text{cum}}}{\tan \alpha}$$

where e_{cum} is the cumulated extension, α is the 60° fault dip, and D_{cum} is the sum of measured throws

$$\mathrm{D}_{\text{cum}} = D1 + D2 + ... + Dn$$

We then used the extension to estimate the amount of strain, ϵ, across each profile by relating the change in profile length (i.e., the extension) to the original pre-extension length by

$$\epsilon = \frac{L_{\text{final}} - L_0}{L_0} = \frac{e_{\text{cum}}}{L_0}$$

where L_{final} is the measured length of the profile (after extension), which we determined by the shortest length that would capture as much faulting for each defined fault group as possible, and L_0 is the original length of the profile before extension:

$$L_0 = L_{\text{final}} - e_{\text{cum}}$$

Strain is a dimensionless value, so we multiply by 100 to get the strain percent value.

3. Results

3.1. Fault Mapping

We mapped a total of 5,115 faults across Ulysses Fossae, with a cumulative length of 32,253 km (Figure 4a). All of the faults are extensional normal faults, which are almost exclusively graben-forming. En échelon fault

21699100, 2023, 5, Downloaded from https://agupubs.onlinelibrary.wiley.com/doi/10.1029/2022JE007633 by Test, Wiley Online Library on [20/07/2023]. See the Terms and Conditions (https://onlinelibrary.wiley.com/terms-and-conditions) on Wiley Online Library for rules of use; OA articles are governed by the applicable Creative Commons License

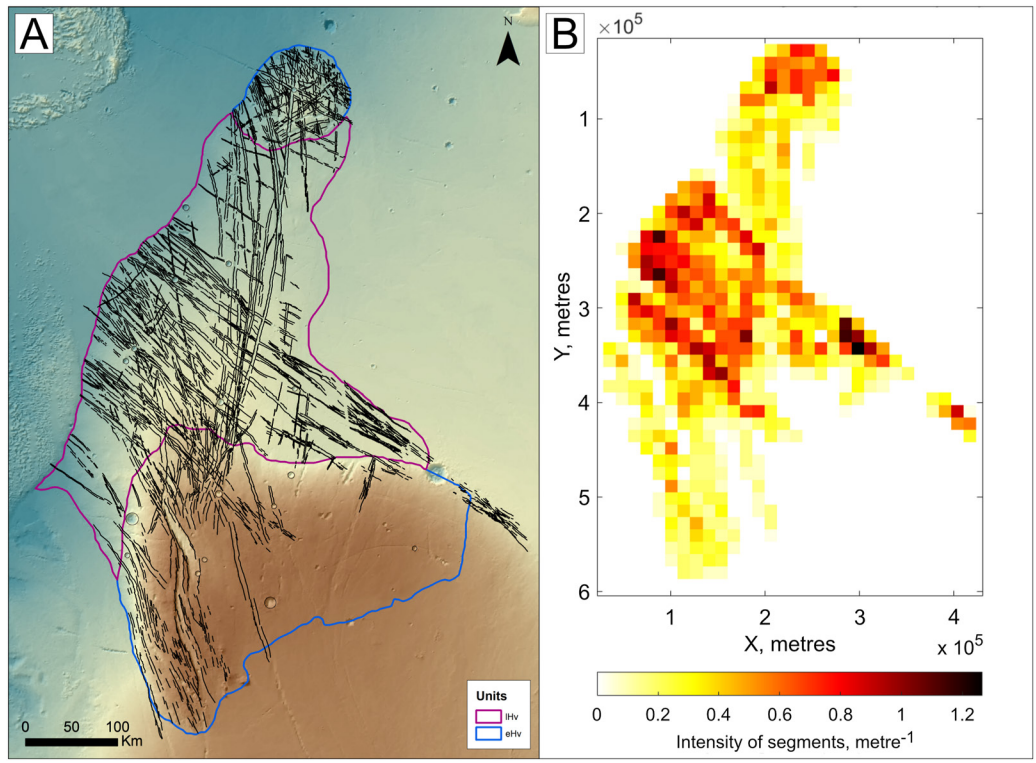

Figure 4. (a) Mapped faults (black) in Ulysses Fossae on Mars Orbiter Laser Altimeter background. Units mapped as eHv (early Hesperian) are outlined in blue, and the unit mapped as lHv (late Hesperian) is outlined in purple. (b) Fault intensity map of all mapped faults. Note the concentration of faults in the UF Dome and the center of UF North.

patterns are common, where grabens are composed of unconnected, discontinuous, but overlapping faults. This high degree of segmentation is reflected in the short average fault lengths (See Table S1 in Supporting Information S1), despite the fact that we observe long, continuous grabens. Spatially, the faulting is not distributed evenly, with regions of higher density in the north and through the center of UF North (Figure 4). The faulting in the UF dome is an area of high fault intensity (Figure 4b), in that there is a larger variety of fault orientations concentrated in a small area, which are arranged in a tight cross-hatch pattern (Figure 4a). The faults in UF North (unit lHv) and UF South (unit eHv) (Figure 1b) are more widely spaced and form long, continuous grabens, which become sparse moving onto UF South. We observe two major fault orientation trends: N and NW. The N-S oriented faults appear larger as their grabens are longer.

Using the previously described criteria, we identified 10 distinct fault groups within our mapped faults, and these were assigned the names G1 to G10 (Table S1 in Supporting Information S1), with G1 being the oldest and G10 youngest. Faults in G1 (Table S1 in Supporting Information S1) trend NE and are contained within the UF Dome unit in Ulysses Fossae. Faults in G2, G3, and G5 show similar NNW orientation, and both groups G2 and G3 have slightly curved faults. Despite their similarities, the distance between the two patches of G2 and G3 warranted their separation. The faults in G4, crosscut all the previous four fault groups, making them the fifth oldest fault system in Ulysses Fossae (Table S1 in Supporting Information S1). G4 faults are present on all three Ulysses Fossae areas and are dominated by a largely N–S orientation, where all the faults lie within a range of 0°–20° (Figure 5). This fault group contains some of the longest grabens in the Ulysses Fossae system, where most have propagated along strike, compared to the faults in G2 and G3 which are more curved. Group G6 has a NNW-oriented fault population and has sparse grabens spread over a large area (Figure 5). The faults making up G7 and G8 have very similar yet discernibly different orientations striking noticeably NW. In both groups, the majority of the faults are located in UF North, with some presence in UF South. These are also the two most populous fault groups (Table S1 in Supporting Information S1), with the highest cumulative lengths of all fault groups. Faults in G9 have an average strike orientation of NE and vary within 10–20°, from the faults in G1 (Figure 5), despite their difference in relative age. The final fault group G10 trends NNW and consists mainly

21699100, 2023, 5, Downloaded from https://agupubs.onlinelibrary.wiley.com/doi/10.1029/2022JE007633 by Test, Wiley Online Library on [20/07/2023]. See the Terms and Conditions (https://onlinelibrary.wiley.com/terms-and-conditions) on Wiley Online Library for rules of use; OA articles are governed by the applicable Creative Commons License

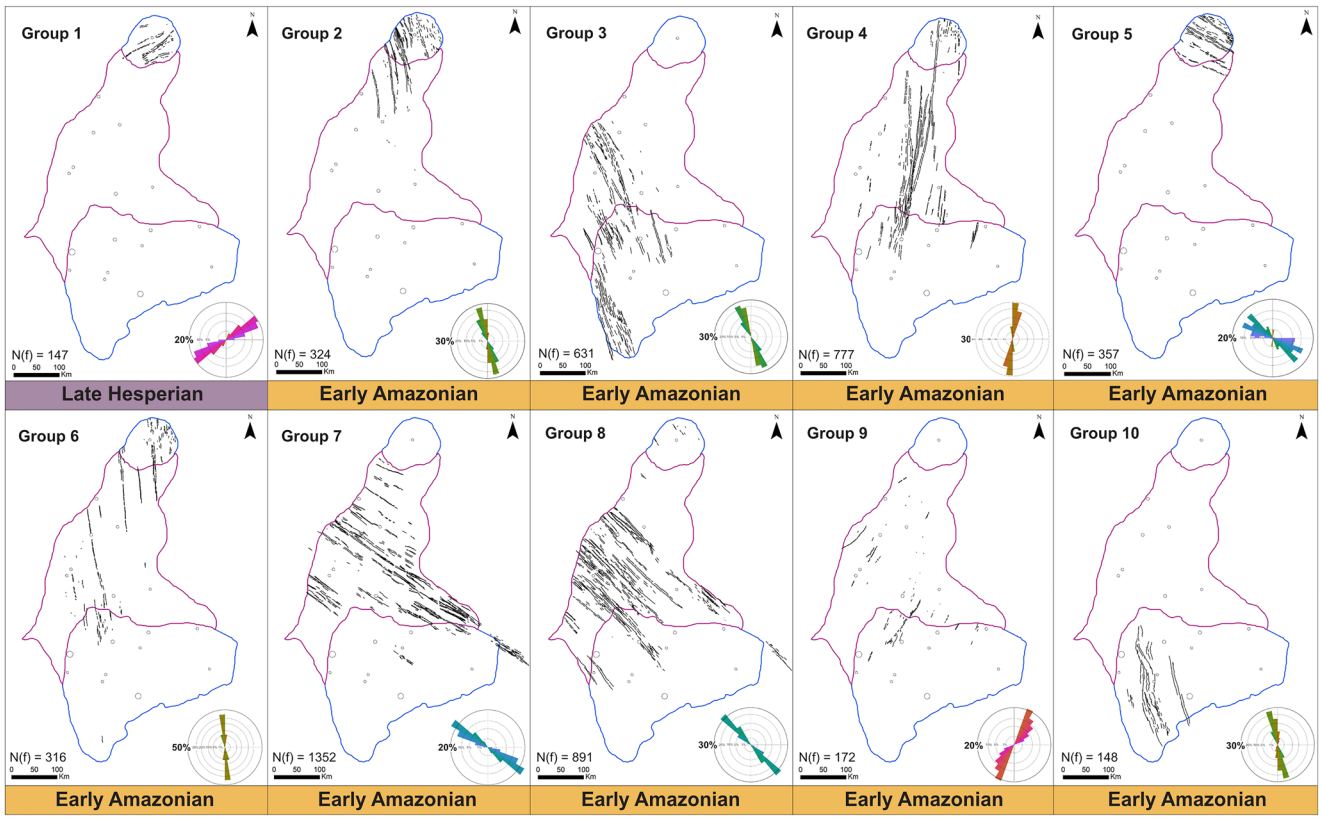

Figure 5. All mapped fault groups in Ulysses Fossae, with rose diagrams depicting the dominant strike orientation of each group. The groups are numbered by relative ages, with Group 1 being the oldest and Group 10 the youngest. The geological age along the bottom refers to the maximum age of the fault group based on the crater statistics derived from the absolute age from this study. N(f) describes the number of faults in each group.

of the large sigmoidal grabens located in UF South. These larger grabens are also accompanied by other en échelon grabens to the east of the main structure (Figure 5). As mentioned, the majority of the mapped faults are purely extensional; however, the G10 faults show changes in orientation with a strike, accompanied by strike-slip components.

3.2. Crater Size-Frequency Distribution

We identified 265 craters with a diameter ≥1 km out of a total of 1,033 mapped craters. Based on the Hartmann (2005) chronology system, we calculated the absolute model ages for the three areas of Ulysses Fossae: UF Dome, UF North and UF South (Figure 1b), resulting in Late Hesperian and Early Amazonian ages for the three units (Table 1). An example of the Crater Size-Frequency Distribution plots is shown in Figure 6.

On the basis of our crater statistics analysis, we assign the UF Dome a Late Hesperian age of 3.4 Ga, making it the oldest in the study area. This is largely consistent with the unit age of Tanaka et al. (2014) for this area (Table 1). UF North and UF South are close in age and we place both units in the early Amazonian period,

Table 1
Ulysses Fossae Absolute Model Ages

AREA NAME	UNIT NAME	(N) CRATERS >1 KM	UNIT AGE	PERIOD
UF DOME	*Early Hesperian volcanic unit (eHv)*	29	3.4 + 0.1/−0.3 Ga	Late Hesperian
UF NORTH	*Late Hesperian volcanic unit (lHv)*	127	2.6 ± 0.2 Ga	Early Amazonian
UF SOUTH	*Early Hesperian volcanic unit (eHv)*	107	2.4 ± 0.2 Ga	Early Amazonian

Note. The unit age results for the three Ulysses Fossae areas (Figure 1b), using crater size-frequency distribution.

21699100, 2023, 5, Downloaded from https://agupubs.onlinelibrary.wiley.com/doi/10.1029/2022JE007633 by Test, Wiley Online Library on [20/07/2023]. See the Terms and Conditions (https://onlinelibrary.wiley.com/terms-and-conditions) on Wiley Online Library for rules of use; OA articles are governed by the applicable Creative Commons License

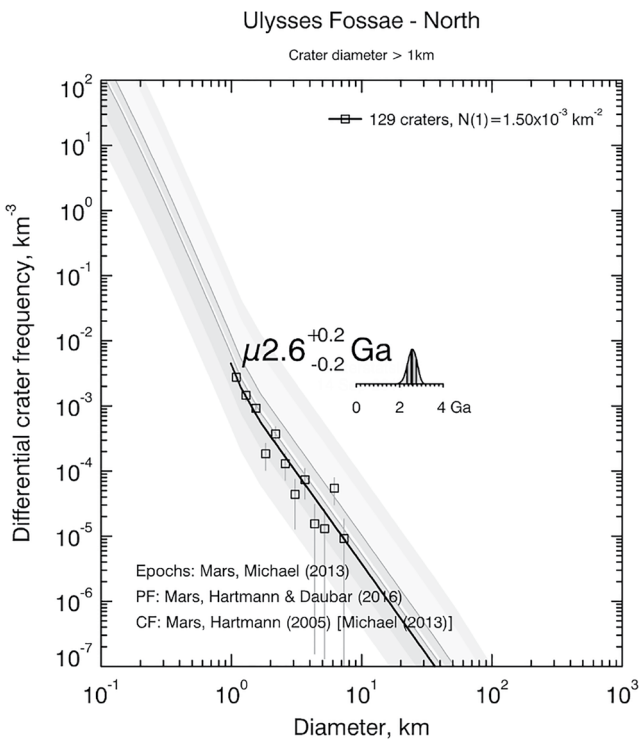

Figure 6. Crater size–frequency distribution (CSFD) plot for UF North, showing a best fit age of 2.6 Ga. See Figure S1 in Supporting Information S1 for all 3 CSFD plots.

making them ~1 Ga younger than recognized in previous studies (Tanaka et al., 2014). Their 2.6 and 2.4 Ga ages are within the uncertainty of each other, making them statistically indistinguishable. To determine their relative age, we therefore relied on the assessment of the number of faults, craters, and surface structures in each. On this basis, we assessed UF South as being the younger of the two units.

A closer study reveals that the UF Dome area has a more degraded appearance than UF South and UF North, with linear features generally appearing less crisp. UF Dome also has many cross-cutting fault directions, high fault intensity (Figure 4b), eroded features, and infilled grabens with smooth floors showing evidence of aeolian landforms formed from the infill material (Figure 7), all of which suggest a relatively older age for this unit. Faults with a pristine appearance that cross the UF Dome belong to Early Amazonian fault groups (G2, G4, G5, and G6).

UF North and UF South differ from UF Dome in that their faults have a sharper appearance, and they lack the infill and other degraded features seen in UF Dome. The UF South unit appears to be the most pristine of the three areas, containing fewer craters and having a lower fault intensity (Figure 4b). This is evident when examining the southern extent of the mapped faults (G3–G9 on Figure 5), where there is a definite lack of fault traces in UF South.

From these absolute model ages, combined with the relative ages determined by cross-cutting relationships, we placed the defined fault groups (Table S1 in Supporting Information S1) into chronological order (Figure 5). The vast majority of faulting (97.11%) occurs in the Early Amazonian, with only one group of Late Hesperian faults (G1). This Late Hesperian group is also NE-trending, which is not a common orientation in Ulysses Fossae.

3.3. Fault Group Sources

3.3.1. Fault Type Assignment

We assessed potential sources for the mapped fault groups using geometrical analysis. Our assigned sources fall into two categories: Regional and Local, based on the main influence on the extension of the faults. In our study,

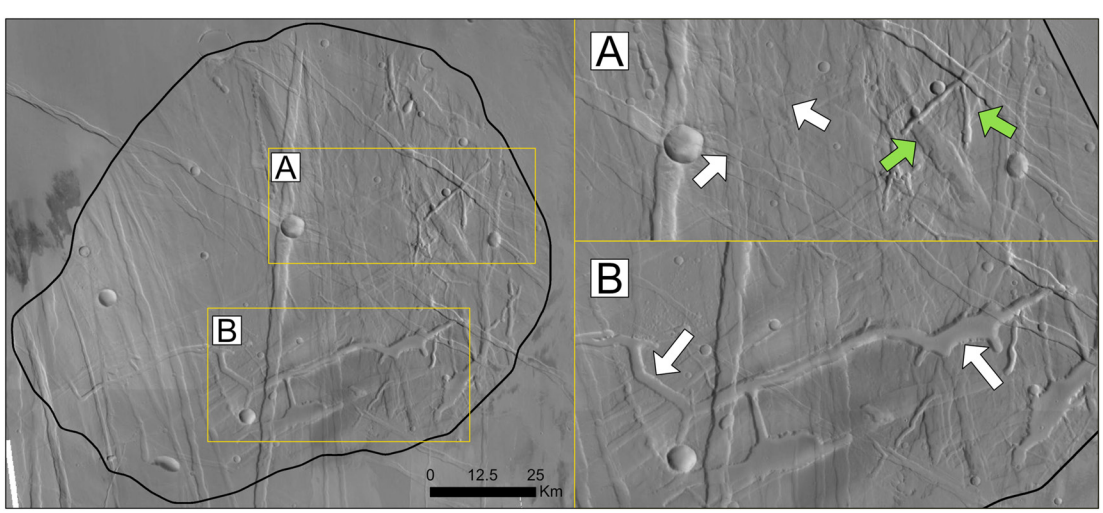

Figure 7. Zoom on the UF Dome in Ulysses Fossae. In Zoom A, the white arrows highlight faint fault traces, which compared to the rest of Ulysses Fossae suggests a combination of infill and erosion, hence the older age. The green arrows highlight an example of overlapping features with faults, craters, and other altered circular features. Zoom B shows an example of an eroded extensional structure with a smooth graben floor, inferred as infilled.

21699100, 2023, 5, Downloaded from https://agupubs.onlinelibrary.wiley.com/doi/10.1029/2022JE007633 by Test, Wiley Online Library on [20/07/2023]. See the Terms and Conditions (https://onlinelibrary.wiley.com/terms-and-conditions) on Wiley Online Library for rules of use; OA articles are governed by the applicable Creative Commons License

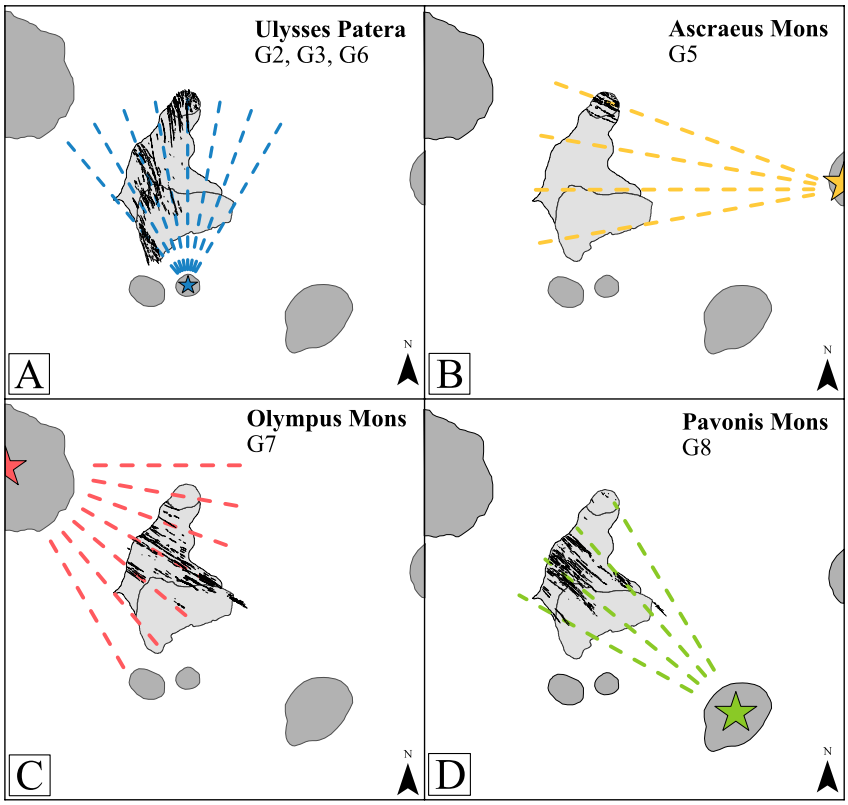

Figure 8. Mapped fault groups (black) with examples of radial orientations (dashed colored lines) from a proximal Volcanic Center (star) in Tharsis. (a) Fault groups 2, 3, and 6 all lining up with the Ulysses Patera volcano to the south. (b) Fault Group 5 lining up with radial orientations from Ascraeus Mons to the East. (c) Fault Group 7 following the Olympus Mons radial orientations, and (d), Group 8 faults following a radial orientation back to the Pavonis Mons volcano. Unit outlines from Tanaka et al. (2014).

fault groups were defined as *Regional* if the orientation of the faults fit the general N-S fault pattern corresponding to the E-W extensional stress expected from the isostatic development of the Tharsis Rise in this area (Banerdt et al., 1982; Carr, 1974; Melosh, 1980).

Fault groups were classified as *Local* if the orientation of the faults did not align with the expected pattern for regional Tharsis activity (i.e., were not oriented N-S) or if their orientation could be traced back radially to a local volcanic center. This pattern is especially obvious in cases where the faults fan outwards.

We then used the orientation-based source of faulting, along with the ages of the fault groups, to define a series of stages encapsulating the volcano-tectonic evolution of Ulysses Fossae.

We identified two fault groups which fit our *Regional* criteria and we thus associate with Tharsis regional extensional stresses. These are groups G4 and G10, both of which trend primarily N-S, following the regional E-W extension. The slight curvature of faults in G4 can be attributed to an influence of local extensional stresses interacting with the regional stress field, with the Biblis Patera volcano as a possible center of deformation.

We define six groups as having a *local* source with a radial relationship to a specific volcanic center. These are groups G2, G3, G5, G6, G7, and G8 (Figure 8), making this the most common source of faults mapped in Ulysses Fossae. G2, G3, and G6 all have an approximately radial orientation to the southern Ulysses Patera volcano. However, in G2 and G3, some faults display slight curvature to the NW in the northern section of each group, suggesting influences from other local stress fields in this area. The faults in groups G5, G7, and G8 have a radial relationship to the three largest volcanoes in the area: Ascraeus Mons (G5), Olympus Mons (G7), and Pavonis Mons (G8).

The faults in groups G1 and G9 are difficult to assign unambiguously within our classification system as they have limited spread and do not fully fit the criteria of either source. While neither G1 nor G9 have an obvious

21699100, 2023, 5, Downloaded from https://agupubs.onlinelibrary.wiley.com/doi/10.1029/2022JE007633 by Test, Wiley Online Library on [20/07/2023]. See the Terms and Conditions (https://onlinelibrary.wiley.com/terms-and-conditions) on Wiley Online Library for rules of use; OA articles are governed by the applicable Creative Commons License

Table 2
Example of Strain Calculations for Group 4 Profiles (Faults in Figure 5)

	D_{cum}	e_{cum}	L_0 (m)	L_{final} (m)	ϵ	%
Profile A	859	495.9	98,204	98,699	0.005	0.51
Profile B	1,086	627.0	90,847	91,474	0.007	0.69
Profile C	991	572.2	71,537	72,109	0.008	0.80
Profile D	561	323.9	51,644	51,968	0.006	0.63
Group 5 average strain %						0.66

Note. ϵ is the calculated strain, with "%" showing the percentage.

radial relationship to any of the surrounding large volcanoes, they can potentially be attributed to the Jovis Tholus volcano, located ~200 km to the NNE of the UF Dome. We thus tentatively assign them as *Local*.

3.4. Strain Measurements

In Table 2, we show an example of the values used in strain calculations for the faults in Group 5 (See Table S2 in Supporting Information S1 for all calculations). The strain percentage results for each fault group are given in Table 3; we were unable to estimate strain amounts for G5 and G9 as the MOLA-HRSC data for those structures were insufficient in resolving all the faults. The strain percentage for the fault groups ranged from a minimum of 0.28% for G6 and a maximum of 2.20% for G10 (Table 3).

Figure 9 shows the maximum strain value for each mapped fault group (Table 3) through time, along with the assigned origin for the fault group. The size of the volcano for the local fault groups (black circles in Figure 9) is also considered. Using this plot, we separate the fault groups into three zones (gray blocks on Figure 6) based on data grouping. The first zone, Zone A, consists of fault groups with strain values below 0.6%, all of which have a radial orientation to the smaller Tharsis volcanoes Ulysses Patera and Jovis Tholus. In Zone B, the strain values range between 0.6% and 2.0%. This zone consists of one fault group (G4) related to regional extension, and two fault groups related to local sources, with faults radially related to the largest volcanoes, Olympus Mons and Pavonis Mons. These three fault groups have the highest measured cumulative lengths. Zone C contains just one fault group (G10), which is the youngest and has the highest strain. G10 peaks at 2.2% strain, more than double the subsequent highest value of 0.94% (G7) and is related to the regional extension of Tharsis.

If all the fault groups are considered together, there is no clear trend in the amount of strain through time. However, by assessing the local and regional groups separately, some discernible trends appear. For the locally sourced groups, we see a change through time from faults linked to smaller, older volcanoes to faults associated with larger, younger volcanoes, with a corresponding increase in strain. While we only have two groups to compare, the regional fault groups also show an increase in strain through time.

4. Discussion

4.1. Ages

We found our geological unit ages to be generally younger than those assigned by Tanaka et al. (2014) (Table 4) in their global study, and the similar Hesperian 3.5 Ga age for UF South determined by Fernández and Ramírez-Caballero (2019). For the UF Dome, our Late Hesperian age agrees with Tanaka et al. (2014), but our numerical age is slightly lower than theirs, although within the uncertainty range (Table 4). We assign both UF North and UF South as Early Amazonian, ~1 Ga younger than the Hesperian ages from Tanaka et al. (2014) for both units (Table 4). Our results indicate that the youngest unit in Ulysses Fossae is UF South, while in the

Table 3
Strain Amounts for Each Measurable Fault Group (G1–G10)

	G1	G2	G3	G4	G5	G6	G7	G8	G9	G10
Profile A	0.44	0.39	0.37	0.51	–	0.28	0.75	0.74	–	2.20
Profile B	0.42	0.33	0.56	0.69	–	0.03	0.94	0.57	–	1.74
Profile C	–	–	–	0.80	–	–	0.78	0.51	–	1.51
Profile D	–	–	–	0.63	–	–	0.63	0.40	–	0.87
Profile E	–	–	–	–	–	–	0.22	0.54	–	–
Profile F	–	–	–	–	–	–	0.46	–	–	–
Average	0.43	0.36	0.47	0.66	–	0.16	0.63	0.55	–	1.58
Max	0.44	0.39	0.56	0.80	–	0.28	0.94	0.74	–	2.20

Note. All values are percentages. The number of profiles for each group was determined by the quality of data for their location. Group 5 and 9 yielded no useable topographic profiles.

21699100, 2023, 5, Downloaded from https://agupubs.onlinelibrary.wiley.com/doi/10.1029/2022JE007633 by Test, Wiley Online Library on [20/07/2023]. See the Terms and Conditions (https://onlinelibrary.wiley.com/terms-and-conditions) on Wiley Online Library for rules of use; OA articles are governed by the applicable Creative Commons License

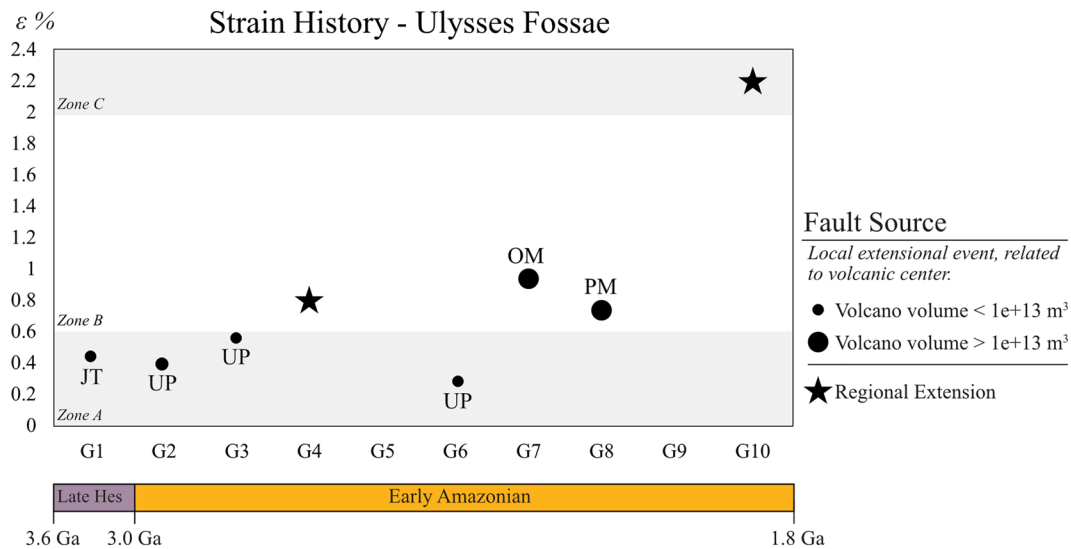

Figure 9. Summary of maximum estimated strain values for the different mapped fault groups through time, along with a circle or star symbol indicating their formation mechanism. No values were measured for G5 and G9. Letters above or below a circle refers to the "local volcano" the faults are radial to; JT = Jovis Tholus, UP = Ulysses Patera, OM = Olympus Mons, PM = Pavonis Mons.

Tanaka et al. (2014) map this was UF North. These differences are likely due to the previous ages being a part of a global-scale study while our work is confined to Ulysses Fossae, which allows for greater, more location-specific detail.

Comparing our results to the Fernández and Ramírez-Caballero (2019) study of UF South, we use a similar method of only using crater diameters >1 km and focus only on the local ages of Ulysses Fossae. Despite the method similarities, we produce an age which is ∼1 Ga younger. This is likely due to the Hartmann (2005) chronology system, where the production function curves for 1 Ga and 3.5 Ga plot very close to each other. This means that the resulting model age is largely affected by even small variations in counted crater frequency, where variations can be caused by differences in image quality and the methods and algorithms used in identifying, counting, measuring, and calculating the statistical outcome.

Our crater-statistics based ages are further supported by the fault and unit morphology of each area, where our results highlighted that the UF dome appears morphologically older, and the UF South appears more pristine and thus younger, fitting the model ages.

A possible explanation for the younger age of UF South in this study lies in an examination of the bounds of the unit defined by Tanaka et al. (2014) (Figure 1b). Within this area, the topography reveals a local high in the terrain (Figure 1b), which continues further south, outside the mapped Tanaka et al. (2014) borders. Given the rounded, lobate edges to the outline of this topographic high, and its proximity to the surrounding volcanoes, we interpret this feature as an Amazonian lava flow likely sourced from one of the surrounding Tharsis Montes, most likely Pavonis or Arsia Mons, based on the flow-lobe orientation. This suggests that Ulysses Fossae experienced an Amazonian resurfacing event. This is further supported by the lack of fault traces and craters within the

Table 4
Comparison of Tanaka et al. (2014) Ages and This Study's (2023) New Cratercount Ages for the Three Mapped Ulysses Fossae Areas UF Dome, UF North and UF South (Figure 1b)

AREA NAME	UNIT NAME	UNIT AGE (2014)	UNIT AGE (2022)	OLD PERIOD (2014)	NEW PERIOD (2022)
UF DOME	*Early Hesperian volcanic unit (eHv)*	3.65 Ga	3.4 + 0.1/−0.3 Ga	Early Hesperian	Late Hesperian
UF NORTH	*Late Hesperian volcanic unit (lHv)*	3.55 Ga	2.6 ± 0.2 Ga	Late Hesperian	Early Amazonian
UF SOUTH	*Early Hesperian volcanic unit (eHv)*	3.65 Ga	2.4 ± 0.2 Ga	Early Hesperian	Early Amazonian

Note. Note the younger ages for areas UF North and UF South.

21699100, 2023, 5, Downloaded from https://agupubs.onlinelibrary.wiley.com/doi/10.1029/2022JE007633 by Test, Wiley Online Library on [20/07/2023]. See the Terms and Conditions (https://onlinelibrary.wiley.com/terms-and-conditions) on Wiley Online Library for rules of use; OA articles are governed by the applicable Creative Commons License

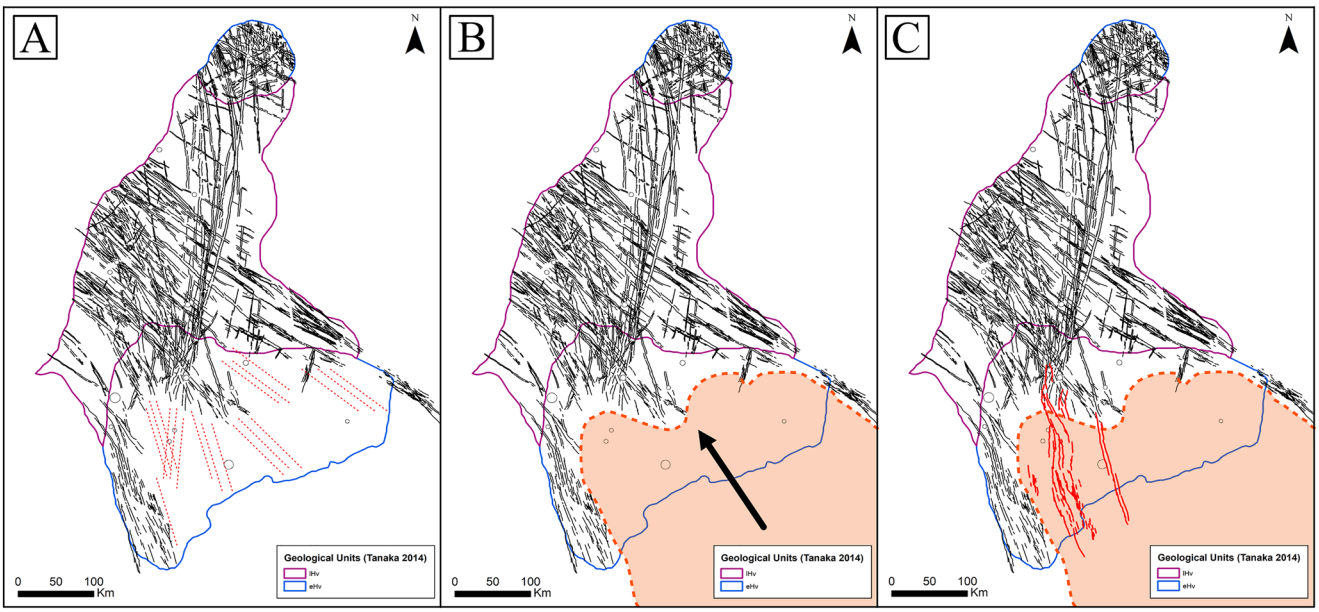

Figure 10. (a) In black are the mapped "original" traces of the faults in Groups 1–9. Dashed red lines show inferred further continuation of the mapped fault traces, when the faulting originally occurred. (b) An Amazonian resurfacing event involving lava covering the southern section of Ulysses Fossae as well as potentially covering some fault traces (the dashed red lines from A). (c) The youngest mapped faults from Group 10 in Ulysses Fossae become active, and the faulting occurred on the more recently emplaced lava.

boundaries of the topographic high in UF South. This resurfacing event potentially covered some of the southern extent of the faults in G1–G9. Following this resurfacing event, another period of extension occurred and produced faults in G10 on top of the younger lava. This interpretation suggests that the crater statistics-derived 2.4 Ga model age for UF South in part reflects a resurfacing event, resulting in a younger age of the unit. This also implies that the current southern border of UF South is inaccurate, and that Ulysses Fossae does not have a defined southern border in the area, but is instead part of a larger, younger Amazonian unit which extends southwards. Figure 10 illustrates the suggested evolution of the UF South region.

4.2. Sources of Fault Trends in Ulysses Fossae

The faults of Ulysses Fossae reflect a long period of varied extensional activity from a combination of local and regional sources.

As mentioned above, the N-S regional fault orientation pattern is attributed to isostasy in the first phase of Tharsis' evolution (Banerdt et al., 1982). This has implications as our results present traces of this mechanism in the early Amazonian, suggesting either a more recent reactivation of the isostasy, which is unlikely to be confined only to the Ulysses Fossae area, or a secondary extensional event, which led the faulting to follow any remnant N-S traces underlying the Amazonian and late Hesperian units.

Faults with radial orientations on Mars have previously been interpreted as the surface expression of dikes which terminated before reaching the surface (Mège & Masson, 1997; Scott et al., 2002). It is inferred that the dikes are controlled by the same deep magma source responsible for the origin of the Tharsis volcanoes (e.g., Cailleau et al., 2005; Dohm et al., 2007) based on their radial orientation to these volcanic centers. We attribute fault groups G1-G3 and G5-G9 as having faulted initiated by radially propagating dikes from local Tharsis volcanoes. Radial extension alone without igneous input, as part of volcano edifice growth, is unlikely to be a source of the radial faulting, due to the large distance (100–800 km) between the mapped faults and the inferred radial centers. Examples of radial diking have been observed on other terrestrial planets, such as Venus and Earth, in addition to other locations on Mars, where dikes have radiated out from a volcanic center (e.g., Cailleau et al., 2005; Grosfils & Head, 1994; Paquet et al., 2007). Both the Martian and Venusian radial diking have evidence of surface faulting, with normal faults creating grabens above the dikes. Multiple studies have linked the formation of radial faults surrounding volcanic centers to the propagation of dikes on both Venus (Ernst et al., 2001; Grosfils & Head, 1994) and Mars (Bouley et al., 2018; Cailleau et al., 2003; Mège et al., 2003; Mège & Masson, 1996; Scott et al., 2002; Wilson & Head III, 2002). The Venusian

21699100, 2023, 5, Downloaded from https://agupubs.onlinelibrary.wiley.com/doi/10.1029/2022JE007633 by Test, Wiley Online Library on [20/07/2023]. See the Terms and Conditions (https://onlinelibrary.wiley.com/terms-and-conditions) on Wiley Online Library for rules of use; OA articles are governed by the applicable Creative Commons License

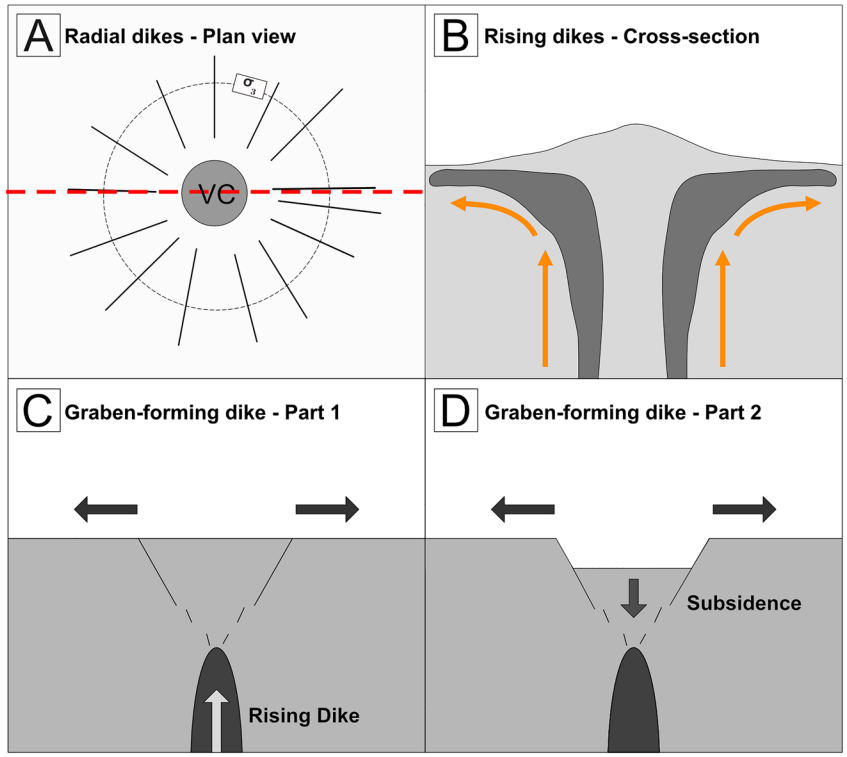

Figure 11. Example of radial diking with a Volcanic Center (VC). (a) Plane view of radial diking from VC. Red dashed line indicates the location of the cross-section in (b), with σ_3 orientation labeled. Modified from Park (2000). (b) Cross-section from A, of upwelling magma from a deep source, forming a radial orientation of dikes from the central volcano. Orange arrows indicate the development of magma flow orientation. (c) Part 1 of dike rising producing grabens. The rising dike produces fractures and faults, enabling the formation of grabens (d).

radial dikes are distinctive as the planet's consistent surface ages make it possible to trace the laterally–extensive, dike-induced faults several kilometers from the center of magma supply (Grosfils & Head, 1994).

On Mars, radial grabens originating from a volcanic center are inferred to be the surface manifestation of mantle plume-related dike intrusion complexes (Bouley et al., 2018; Schultz et al., 2004). Figure 11b shows a cross-section along the dotted red line in Figure 11a and shows an idealized example of a magma leading to a radial dike pattern, which is characteristically considered to flow upwards above the melting source, at which point the orientation changes and the magma will then expand laterally toward outer regions (Mège et al., 2003; Poland et al., 2008). In instances where the least compressive stress ($\sigma 3$) is circular surrounding a volcanic center, such as during magma upwelling, dikes will form in a radial pattern, orthogonal to the $\sigma 3$ stress orientations (Park, 2000) (Figure 11a).

In some instances, an upwards-propagating dike will not reach the surface, but the tensile stress generated by the now-arrested dike tip can initiate fractures, which can develop into normal faulting on the surface (Figures 11c and 11d) (Ernst et al., 2001; Gudmundsson, 2020; Mège & Masson, 1996). It is, however, the consensus that on Earth, dikes alone do not generate extensive surface faulting, such as that observed on Mars and Venus, so that dike-induced deformation has to occur in tandem with regional-scale crustal tension (Gudmundsson, 2020). This scenario is also possible on Mars for regions such as Tharsis, which have local volcanic diking sources superposed on a significant regional stress field. Consequently, the distribution of extensional faults in the Tharsis region can be treated as stress-trajectory maps (Figure 8), which can be traced back to their source volcano based on a plume tectonics model (Mège & Masson, 1996).

The faults mapped in this study represent a complex system where radial diking appears to be the main driver of faulting in Ulysses Fossae. As very little older material (Hesperian and Noachian) is preserved in the area, it is not surprising that most of tectonic activity recorded in the faults of Ulysses Fossae are related to Amazonian volcanism, and that we have minimal evidence of older large-scale events. However, it is important to note that our attribution of fault groups as being primarily sourced from either regional extension or local dike emplacement

21699100, 2023, 5, Downloaded from https://agupubs.onlinelibrary.wiley.com/doi/10.1029/2022JE007633 by Test, Wiley Online Library on [20/07/2023]. See the Terms and Conditions (https://onlinelibrary.wiley.com/terms-and-conditions) on Wiley Online Library for rules of use; OA articles are governed by the applicable Creative Commons License

does not exclude the interaction of these two sources or the influence of other sources of stress. It is in fact very likely that the local and regional processes interact, particularly in cases where faulting from regional extension is influenced by diking originating from the Tharsis volcanoes, such as fault group G4. This process is also seen on Earth in the Afar rift, where the dike intrusion influences an area undergoing regional extension (Calais et al., 2008), resulting in oblique fault structures (La Rosa et al., 2019).

4.2.1. Oblique Faulting

The faults of G10 are attributed to the regional extension and largely follow an overall N-S trend. They have a unique geometry among the Ulysses Fossae faults that reflects the influence of additional mechanisms in their development. Specifically, the curved and sigmoidal morphology of the G10 faults indicates oblique faulting processes, with signs of simultaneous strike-slip and dip-slip movements. This distinct shape of the faults in G10 is interpreted to be a result of the influence of older fault patterns in Ulysses Fossae, which are reactivated during later faulting. The large size of the graben indicates large-scale regional extension, with the N-S orientation of the faults allowing for a partial reactivation of the previously established fault patterns of G3 and G4, creating the distinctive sigmoidal shape for the largest faults in the population (Figure 5). The extension for the G10 faults is therefore not purely orthogonal to the N-S general extension, reflecting the transtensional kinematics in UF South, similar to the interpretations of Fernández and Ramírez-Caballero (2019). The difference in elevation between UF North and UF South suggests a lava flow with a maximum thickness of ∼2 km, which has allowed the extensional event for G10, to follow the patterns of G3 and G4 under the lava (Figure 12).

This may also be why we detected some traces of G3 and G4 faults on top of the thinner edges of UF South. The strain values calculated for G10 are significantly larger than the other groups, with a maximum strain of 2.2% (Table 3). This higher strain reflects the greater extension accommodated by the large grabens, which is potentially aided by the pre-existing structural weaknesses from the previous fault trends (Figure 12).

It is important to note that the overall N-S Tharsis extensional trend, determined by Barnerdt et al. (1982), has likely varied in orientations through time, and through the Tharsis structure. A kinematic analysis was performed on UF South faults in Fernández and Ramírez-Caballero (2019), where they determined a regional extension of is NE-SW, with important local variations from E-W to NNE-SSW. This is in accordance with our interpretations of the G10 faults as a reactivation and oblique tectonic structure and is further observed in the map en échelon structures in Ulysses Fossae, which hints at slight stress orientation changes through the development of the faults.

4.3. Structural Evolution of Ulysses Fossae

Combining the fault groups, ages, and sources together, we present an overview of the main events in the structural evolution of Ulysses Fossae, as recorded in the mapped faults and unit ages and morphology.

4.3.1. Stage 1: Late Hesperian

The first recorded stage in Ulysses Fossae is dominated by a single event, a local NW-SE extension, potentially related to diking activity from the Jovis Tholus volcano, which produced faults in G1. These faults are exclusive to the UF Dome.

4.3.2. Stage II: Early Amazonian, Local Extension 1

The early Amazonian units in UF North and presumably underneath UF South were deposited, leaving the only traces of G1 preserved in the elevated UF Dome. This was followed by activity from several local volcanic centers. Diking from Ulysses Patera initiated faulting in G2 and again in G3, potentially in the presence of another local or regional stress field, resulting in the slightly curved faulting.

4.3.3. Stage III: Early Amazonian, Regional Extension

Regional E-W extension followed this period of local events, and potentially interacted with structural weaknesses related to Biblis Patera to create the faults in G4.

4.3.4. Stage IV: Early Amazonian, Local Extension 2

The fourth stage of faulting in Ulysses Fossae is also contained within the early Amazonian and represents the main period of recorded faulting. Faults from this stage are radial to proximal volcanic centers, reflecting the diking activity associated with various local volcanoes.

21699100, 2023, 5, Downloaded from https://agupubs.onlinelibrary.wiley.com/doi/10.1029/2022JE007633 by Test, Wiley Online Library on [20/07/2023]. See the Terms and Conditions (https://onlinelibrary.wiley.com/terms-and-conditions) on Wiley Online Library for rules of use; OA articles are governed by the applicable Creative Commons License

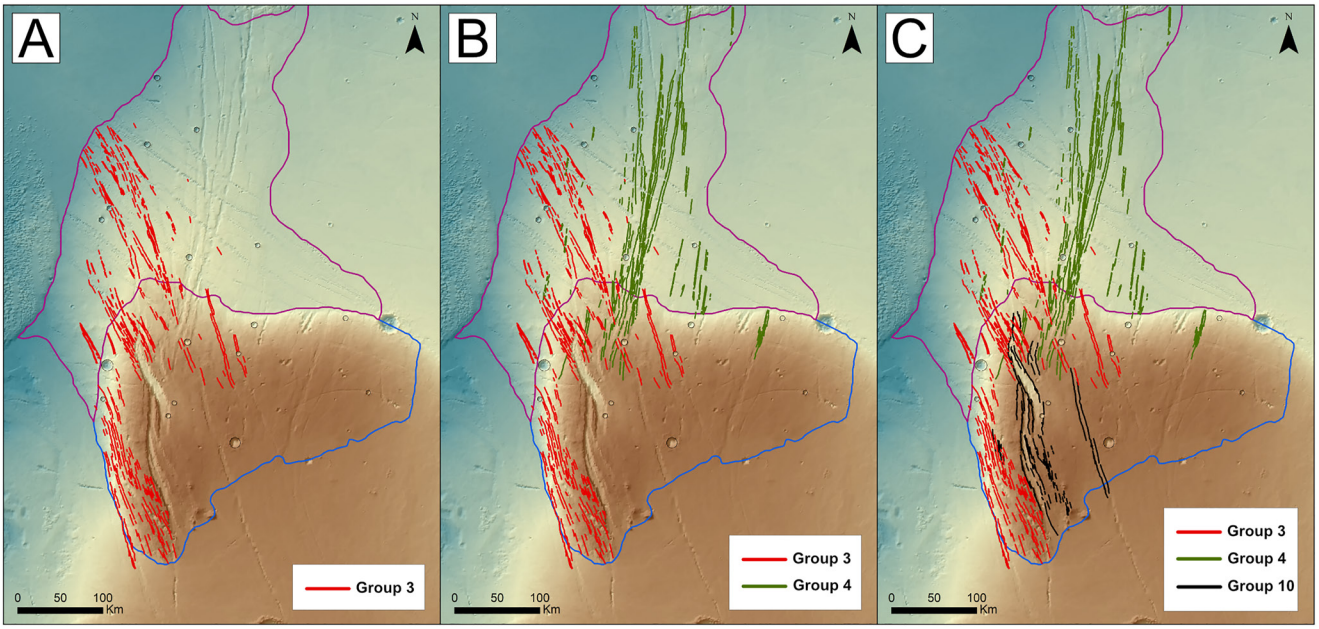

Figure 12. Group 3 and Group 4 faults, which influenced the orientation of the Group 10 faults, during their evolution. (a) shows the oldest activity of the 2 fault groups influencing the orientation of Group 10, with Group 3 being active in the Early Amazonian. Following that in (b), the faults in Group 4 become active due to regional Tharsis extension. Finally, in (c), a regional E-W extension event becomes active in the southern part of Ulysses Fossae, but the pre-existing fabric of the faults from Groups 3 and 4 influences a partial reactivation of the faults, resulting in the faults in Group 10 creating a sigmoidal pattern, and not the N-S oriented faults that are expected.

First, dikes from Ascraeus Mons produced the G5 faults, followed by the final activity related to Ulysses Patera diking forming the faults in G6. Following this, Olympus Mons produced radial dikes which created the faults in G7. Finally, diking activity from Pavonis Mons initiated the faults in G8. The measured strain from this period reflects the fact that the two biggest volcanoes were active (Figure 9).

4.3.5. Stage V: Early Amazonian, Local Extension 3

An extensional event, potentially related to diking from Jovis Tholus, produced the scattered faults of G9. This was followed by a series of lava flows which surrounded Ulysses Fossae, defining the north, east and western outlines of the UF Dome and UF North units. These flows were likely sourced from Olympus Mons to the west, and along the eastern boundary, by regional fissure and vent systems (Tanaka et al., 2014), and as a result covered any faults which may have extended beyond the current unit boundaries.

4.3.6. Stage VI: Early Amazonian Extension and Reactivation

Another early Amazonian lava flow covers the area, this time from the south, covering any pre-existing faults. This flow was likely sourced from one of the Tharsis Montes. A regional E-W extension event facilitated the initiation of the G10 faults, which reactivated the paths of faults from G3 and G4, creating a large oblique fault structure in UF South.

4.4. Ulysses Fossae and Tharsis Development

Assuming the edifice age of the volcano to be the most recent activity of the volcano, an early Amazonian age for diking related to Olympus Mons, Pavonis Mons, and Ascraeus Mons is consistent with previous mapping of the area (Tanaka et al., 2014), which assigns an Amazonian age to each edifice. For the smaller volcanoes Ulysses Patera, Biblis Patera and Jovis Tholus, the Amazonian activity is more surprising, as their most recent surface activity is attributed to the Hesperian (Tanaka et al., 2014), though a more focused study on the volcanoes themselves has determined Amazonian ages for the Ulysses Patera's caldera, indicating a more recent activity (Robbins et al., 2011). However, disregarding the volcanic edifice itself, a recent study by Richardson et al. (2021) linked a number of observed volcanic vents in Tharsis to the surrounding volcanoes, determining that the Ulysses Fossae

21699100, 2023, 5, Downloaded from https://agupubs.onlinelibrary.wiley.com/doi/10.1029/2022JE007633 by Test, Wiley Online Library on [20/07/2023]. See the Terms and Conditions (https://onlinelibrary.wiley.com/terms-and-conditions) on Wiley Online Library for rules of use; OA articles are governed by the applicable Creative Commons License

magma system may have been active as recently as the Early Late Amazonian (Richardson et al., 2021), validating the Amazonian ages determined in our study.

Despite 5 of our stages occurring during the Early Amazonian, we are not suggesting a contemporaneous formation of all the fault groups during that time. The fault stages are interpreted as sequential events on the basis of the different group orientations, which indicate changes in the primary stress orientations, and the numerous clear cross-cutting relationships, which indicate separate events.

The complexity of the subsurface magmatic systems related to the nearby Tharsis volcanoes, which is recorded in the variously oriented faults in Ulysses Fossae, makes it difficult to distinguish specific events within the larger scheme of the evolution of the Tharsis volcanic province. This is particularly challenging in Ulysses Fossae as most of the faulting events take place during the Amazonian, during the fifth stage of activity of the Tharsis Superplume (Dohm et al., 2007). However, this peak of sustained magmatism, with periodic pulses of diking and subsequent faulting, which is recorded in Ulysses Fossae, provides a constraint on the intense activity taking place during the Amazonian. Considering the Tharsis region as a whole, our absolute age results do agree with recent studies' conclusions that the period of active tectonism experienced in the Tharsis volcanic province has indeed extended into the Amazonian (Bouley et al., 2018), where we add the majority of the faults in Ulysses Fossae to this period, with the added relative distinction between the sources of tectonic activity between the Tharsis volcanoes. Previous studies by Anderson et al. (2001) and Tanaka et al. (1991) similarly identified the main fault activity in Ulysses Fossae to occur before faulting related to Olympus Mons and Pavonis Mons, in concurrence with our relative age results. However, in those studies, faults related to Olympus Mons and Pavonis Mons are not identified within the Ulysses Fossae area (Anderson et al., 2001). This also means that our results vary in terms of absolute ages, where Anderson et al. (2001) and Tanaka et al. (1991) assign an Early Hesperian age to all Ulysses Fossae fault activity, and a Late Hesperian–Early Amazonian age to the Olympus Mons and Pavonis Mons activity.

5. Conclusions

Through our fault mapping of Ulysses Fossae, we identified and analyzed 10 fault groups, which together illustrate several stages of structural activity in the Ulysses Fossae region. Results from relative and absolute model age analysis indicate a complex history involving radial faulting generated by dikes from the surrounding volcanoes (Olympus Mons, Ascraeus Mons, Pavonis Mons, Ulysses Patera and tentatively Jovis Tholus), later reactivation of pre-existing fault populations, and influence from the regional extension related to the Tharsis development. We determine a range of maximum strain values between 0.4%–2.2%, where 2.2% from G10 are significantly higher than the rest of the groups, reflecting a relatively greater extension. Additionally, considered separately, both the local and regional sourced fault groups tend to increase in strain with time.

The faulting in Ulysses Fossae has occurred interspersed with Amazonian-aged lava-emplacement events and thus only records activity since ∼3 Ga ago. The intense extensional faulting associated with the Tharsis volcanoes, including what appears to be multiple extensional events associated with a single volcano, Ulysses Patera, points to the Tharsis volcanotectonic systems being active for longer than previously determined.

Our work provides important background necessary to further unravel the complex tectonic history of the Tharsis volcanic province. Further work will include mapping and comparing other volcanotectonic structures in Tharsis, such as Alba Mons, to the results presented here, ultimately in order to better understand the history of volcanism and tectonism on Mars.

Data Availability Statement

The shapefile of the mapped faults and craters in this study is available for free download from Zenodo: craters (Shahrzad, 2022a), faults (Shahrzad, 2022b). We also provide the .diam CraterTools files for input in Craterstats in Zenodo (Shahrzad, 2023). The CTX images (Malin et al., 2007) used in this study can be downloaded from NASA's PDS Geoscience Node at https://pds-imaging.jpl.nasa.gov/portal/mro_mission.html and the MOLA-HRSC DEM v2 used to generate topographic profiles is available from USGS' Astropedia Catalog (Fergason et al., 2018). The software used in this research is available to download for free. FracPaQ (Healy et al., 2017) is available for download via Github, and Craterstats 2.0 is available via the Freie Universität Berlin at https://www.geo.fu-berlin.de/en/geol/fachrichtungen/planet/software/index.html.

21699100, 2023, 5, Downloaded from https://agupubs.onlinelibrary.wiley.com/doi/10.1029/2022JE007633 by Test, Wiley Online Library on [20/07/2023]. See the Terms and Conditions (https://onlinelibrary.wiley.com/terms-and-conditions) on Wiley Online Library for rules of use; OA articles are governed by the applicable Creative Commons License

Acknowledgments
S. Shahrzad is funded by the National Environmental Research Council Panorama Doctoral Training Partnership NE/S007458/1. We thank NASA and ESA for the free access to Martian data through NASA's Planetary Data System (PDS).

References

Anderson, R. C., Dohm, J. M., Golombek, M. P., Haldemann, A. F. C., Franklin, B. J., Tanaka, K. L., et al. (2001). Primary centers and secondary concentrations of tectonic activity through time in the Western hemisphere of Mars. *Journal of Geophysical Research*, *106*(E9), 20563–20585. https://doi.org/10.1029/2000JE001278

Banerdt, W. B., Phillips, R. J., Sleep, N. H., & Saunders, R. S. (1982). Thick shell tectonics on one-plate planets: Applications to Mars. *Journal of Geophysical Research*, *87*(B12), 9723–9733. https://doi.org/10.1029/JB087iB12p09723

Barlow, N. G. (2008). *Mars, an introduction to its interior, surface and atmosphere*. Cambridge University Press.

Bouley, S., Baratoux, D., Paulien, N., Missenard, Y., & Saint-Bézar, B. (2018). The revised tectonic history of Tharsis. *Earth and Planetary Science Letters*, *488*, 126–133. https://doi.org/10.1016/j.epsl.2018.02.019

Cailleau, B., Walter, T. R., Janle, P., & Hauber, E. (2003). Modeling volcanic deformation in a regional stress field: Implications for the formation of graben structures on Alba Patera, Mars. *Journal of Geophysical Research*, *108*(E12), 5141. https://doi.org/10.1029/2003JE002135

Cailleau, B., Walter, T. R., Janle, P., & Hauber, E. (2005). Unveiling the origin of radial grabens on Alba Patera volcano by finite element modelling. *Icarus*, *176*(1), 44–56. https://doi.org/10.1016/j.icarus.2005.01.017

Calais, E., d'Oreye, N., Albaric, J., Deschamps, A., Delvaux, D., Déverchère, J., et al. (2008). Strain accommodation by slow slip and dyking in a youthful continental rift, East Africa. *Nature*, *456*(7223), 783–787. Article 7223. https://doi.org/10.1038/nature07478

Carr, M. H. (1974). Tectonism and volcanism of the Tharsis region of Mars. *Journal of Geophysical Research*, *79*(26), 3943–3949. https://doi.org/10.1029/JB079i026p03943

Carr, M. H., & Head, J. W. (2010). Geologic history of Mars. *Earth and Planetary Science Letters*, *294*(3), 185–203. https://doi.org/10.1016/j.epsl.2009.06.042

De Blasio, F. V. (2018). The pristine shape of Olympus Mons on Mars and the subaqueous origin of its aureole deposits. *Icarus*, *302*, 44–61. https://doi.org/10.1016/j.icarus.2017.11.003

Dohm, J. M., Baker, V. R., Maruyama, S., & Anderson, R. C. (2007). Traits and evolution of the Tharsis Superplume, Mars. In D. A. Yuen, S. Maruyama, S.-I. Karato, & B. F. Windley (Eds.), *Superplumes: Beyond plate tectonics* (pp. 523–536). Springer Netherlands. https://doi.org/10.1007/978-1-4020-5750-2_17

Ernst, R., Grosfils, E., & Mège, D. (2001). Giant dike swarms: Earth, Venus, and Mars. *Annual Review of Earth and Planetary Sciences*, *29*(1), 489–534. https://doi.org/10.1146/annurev.earth.29.1.489

Fergason, R. L., Hare, T. M., & Laura, J. (2018). HRSC and MOLA blended digital elevation model at 200m v2. [Map] [Dataset]. Astrogeology PDS Annex, U.S. Geological Survey. Retrieved from https://astrogeology.usgs.gov/search/map/Mars/Topography/HRSC_MOLA_Blend/Mars_HRSC_MOLA_BlendDEM_Global_200mp

Fernández, C., & Ramírez-Caballero, I. (2019). Evaluating transtension on Mars: The case of Ulysses Fossae, Tharsis. *Journal of Structural Geology*, *125*, 325–333. https://doi.org/10.1016/j.jsg.2018.05.009

Grosfils, E. B., & Head, J. W. (1994). The global distribution of giant radiating dike swarms on Venus: Implications for the global stress state. *Geophysical Research Letters*, *21*(8), 701–704. https://doi.org/10.1029/94GL00592

Gudmundsson, A. (2020). Volcanotectonics—Understanding the structure, deformation and dynamics of volcanoes. https://doi.org/10.1017/9781139176217

Hartmann, W. K. (2005). Martian cratering 8: Isochron refinement and the chronology of Mars. *Icarus*, *174*(2), 294–320. https://doi.org/10.1016/j.icarus.2004.11.023

Hartmann, W. K., & Daubar, I. J. (2016). Martian cratering 11. Utilizing decameter scale crater populations to study Martian history. *Meteoritics & Planetary Sciences*, *52*(3), 493–510. https://doi.org/10.1111/maps.12807

Hauber, E., & Kronberg, P. (2005). The large Thaumasia graben on Mars: Is it a rift? *Journal of Geophysical Research*, *110*(E7), E07003. https://doi.org/10.1029/2005JE002407

Healy, D., Rizzo, R. E., Cornwell, D. G., Farrell, N. J. C., Watkins, H., Timms, N. E., et al. (2017). FracPaQ: A MATLAB™ toolbox for the quantification of fracture patterns. [Software]. Journal of Structural Geology, *95*, 1–16. https://doi.org/10.1016/j.jsg.2016.12.003

Jenness, J. (2011). *Tools for graphics and shapes*. Jenness Enterprises.

Kneissl, T., van Gasselt, S., & Neukum, G. (2011). Map-projection-independent crater size-frequency determination in GIS environments—New software tool for ArcGIS. *Planetary and Space Science*, *59*(11), 1243–1254. https://doi.org/10.1016/j.pss.2010.03.015

La Rosa, A., Pagli, C., Keir, D., Sani, F., Corti, G., Wang, H., & Possee, D. (2019). Observing oblique slip during rift linkage in Northern Afar. *Geophysical Research Letters*, *46*(19), 10782–10790. https://doi.org/10.1029/2019GL084801

Malin, M. C., Bell, J. F., Cantor, B. A., Caplinger, M. A., Calvin, W. M., Clancy, R. T., et al. (2007). Context Camera investigation on board the Mars reconnaissance orbiter. [Dataset]. Journal of Geophysical Research, *112*(E5), E05S04. https://doi.org/10.1029/2006JE002808

McGovern, P. J., Smith, J. R., Morgan, J. K., & Bulmer, M. H. (2004). Olympus Mons aureole deposits: New evidence for a flank failure origin. *Journal of Geophysical Research*, *109*(E8), E08008. https://doi.org/10.1029/2004JE002258

Mège, D., Cook, A. C., Garel, E., Lagabrielle, Y., & Cormier, M.-H. (2003). Volcanic rifting at Martian grabens. *Journal of Geophysical Research*, *108*(E5), 5044. https://doi.org/10.1029/2002JE001852

Mège, D., & Masson, P. (1996). A plume tectonics model for the Tharsis province, Mars. *Planetary and Space Science*, *44*(12), 1499–1546. https://doi.org/10.1016/S0032-0633(96)00113-4

Mège, D., & Masson, P. (1997). Graben formation and dike emplacement on Earth and other planets. (Vol. *28*, pp. 929).

Melosh, H. J. (1980). Tectonic patterns on a reoriented planet: Mars. *Icarus*, *44*(3), 745–751. https://doi.org/10.1016/0019-1035(80)90141-4

Michael, G. G. (2013). Planetary surface dating from crater size–frequency distribution measurements: Multiple resurfacing episodes and differential isochron fitting. *Icarus*, *226*(1), 885–890. https://doi.org/10.1016/j.icarus.2013.07.004

Michael, G. G., Kneissl, T., & Neesemann, A. (2016). Planetary surface dating from crater size-frequency distribution measurements: Poisson timing analysis. *Icarus*, *277*, 279–285. https://doi.org/10.1016/j.icarus.2016.05.019

Michael, G. G., & Neukum, G. (2010). Planetary surface dating from crater size-frequency distribution measurements: Partial resurfacing events and statistical age uncertainty. *Earth and Planetary Science Letters*, *294*(3–4), 223–229. https://doi.org/10.1016/j.epsl.2009.12.041

Morris, E. C., & Tanaka, K. L. (1994). Geologic maps of the Olympus Mons region of Mars. *Internet Message Access Protocol*. https://doi.org/10.3133/i2327

Paquet, F., Dauteuil, O., Hallot, E., & Moreau, F. (2007). Tectonics and magma dynamics coupling in a dyke swarm of Iceland. *Journal of Structural Geology*, *29*(9), 1477–1493. https://doi.org/10.1016/j.jsg.2007.06.001

Park, R. G. (2000). *Foundations of structural geology* (3rd ed.). Chapman & Hall.

Plescia, J. B. (2004). Morphometric properties of Martian volcanoes. *Journal of Geophysical Research*, *109*(E3), E03003. https://doi.org/10.1029/2002JE002031

21699100, 2023, 5, Downloaded from https://agupubs.onlinelibrary.wiley.com/doi/10.1029/2022JE007633 by Test, Wiley Online Library on [20/07/2023]. See the Terms and Conditions (https://onlinelibrary.wiley.com/terms-and-conditions) on Wiley Online Library for rules of use; OA articles are governed by the applicable Creative Commons License

Poland, M. P., Moats, W. P., & Fink, J. H. (2008). A model for radial dike emplacement in composite cones based on observations from Summer Coon volcano, Colorado, USA. *Bulletin of Volcanology*, *70*(7), 861–875. https://doi.org/10.1007/s00445-007-0175-9

Polit, A. T., Schultz, R. A., & Soliva, R. (2009). Geometry, displacement–length scaling, and extensional strain of normal faults on Mars with inferences on mechanical stratigraphy of the Martian crust. *Journal of Structural Geology*, *31*(7), 662–673. https://doi.org/10.1016/j.jsg.2009.03.016

Richardson, J. A., Bleacher, J. E., Connor, C. B., & Glaze, L. S. (2021). Small volcanic vents of the Tharsis volcanic province, Mars. *Journal of Geophysical Research: Planets*, *126*(2), e2020JE006620. https://doi.org/10.1029/2020JE006620

Robbins, S. J., Achille, G. D., & Hynek, B. M. (2011). The volcanic history of Mars: High-resolution crater-based studies of the calderas of 20 volcanoes. *Icarus*, *211*(2), 1179–1203. https://doi.org/10.1016/j.icarus.2010.11.012

Schultz, R. A., Okubo, C. H., Goudy, C. L., & Wilkins, S. J. (2004). Igneous dikes on Mars revealed by Mars orbiter laser altimeter topography. *Geology*, *32*(10), 889–892. https://doi.org/10.1130/G20548.1

Scott, D., & Dohm, J. (1990). Faults and ridges—Historical development in Tempe terra and Ulysses Patera regions of Mars. *Proceedings of the twentieth lunar and planetary science conference*.

Scott, D. H., Tanaka, K. L., & Kozak, R. (1986). Geologic map of the western equatorial region of Mars.

Scott, E. D., Wilson, L., & Head, J. W., III. (2002). Emplacement of giant radial dikes in the northern Tharsis region of Mars. *Journal of Geophysical Research*, *107*(E4), 3-1–3-10. https://doi.org/10.1029/2000JE001431

Shahrzad, S. (2022a). Ulysses Fossae crater catalogue [Dataset]. Zenodo. https://doi.org/10.5281/zenodo.7220715

Shahrzad, S. (2022b). Ulysses Fossae fault catalogue [Dataset]. Zenodo. https://doi.org/10.5281/zenodo.7220699

Shahrzad, S. (2023). Ulysses Fossae craterstats input [Dataset]. Zenodo. https://doi.org/10.5281/zenodo.7657313

Tanaka, K. L., Golombek, M. P., & Banerdt, W. B. (1991). Reconciliation of stress and structural histories of the Tharsis region of Mars. *Journal of Geophysical Research*, *96*(E1), 15617–15633. https://doi.org/10.1029/91JE01194

Tanaka, K. L., Skinner, J. A., Jr., Dohm, J. M., Irwin, R. P., III., Kolb, E. J., Fortezzo, C. M., et al. (2014). *Geologic map of Mars*. Scientific Investigations Map.

Thomas, P. G., & Allemand, P. (1993). Quantitative analysis of the extensional tectonics of Tharsis Bulge, Mars: Geodynamic implications. *Journal of Geophysical Research*, *98*(E7), 13097–13108. https://doi.org/10.1029/93JE01326

Werner, S. C., Ivanov, B. A., & Neukum, G. (2009). Theoretical analysis of secondary cratering on Mars and an image-based study on the Cerberus Plains. *Icarus*, *200*(2), 406–417. https://doi.org/10.1016/j.icarus.2008.10.011

Wilson, L., & Head, J. W., III. (2002). Tharsis-radial graben systems as the surface manifestation of plume-related dike intrusion complexes: Models and implications. *Journal of Geophysical Research*, *107*(E8), 1-1–1-24. https://doi.org/10.1029/2001JE001593

21699100, 2023, 5, Downloaded from https://agupubs.onlinelibrary.wiley.com/doi/10.1029/2022JE007633 by Test, Wiley Online Library on [20/07/2023]. See the Terms and Conditions (https://onlinelibrary.wiley.com/terms-and-conditions) on Wiley Online Library for rules of use; OA articles are governed by the applicable Creative Commons License